THE ASTROPHYSICAL JOURNAL, 409:282–298, 1993 May 20

THE PHYSICAL STRUCTURE OF ORION-KL ON 2500 AU SCALES USING THE *K*-DOUBLET TRANSITIONS OF FORMALDEHYDE

JEFFREY G. MANGUM
Steward Observatory, Submillimeter Telescope Observatory, University of Arizona, Tucson, AZ 85721,[1]
Department of Astronomy, University of Texas, Austin, and National Radio Astronomy Observatory[2]

ALWYN WOOTTEN
National Radio Astronomy Observatory,[2] Edgemont Road, Charlottesville, VA 22903

AND

RICHARD L. PLAMBECK
Radio Astronomy Laboratory, University of California, Berkeley, CA 94720
Received 1992 August 3; accepted 1992 November 13

ABSTRACT

The physical characteristics of a molecular cloud which relate most closely to star formation within it occur on the finest spatial scales. Generally, several transitions of a specific molecule must be mapped to securely determine molecular cloud physics. Toward this goal, interferometric observations of the $1_{10} \rightarrow 1_{11}$ and $5_{14} \rightarrow 5_{15}$ transitions of H_2CO have been made toward the Orion-KL molecular cloud. With synthesized beamwidths of 5"1 (2400 AU) and 7"6 (3500 AU), respectively, we identify emission from the "hot core," "compact ridge," and "northern cloud" regions. We also detect $1_{10} \leftarrow 1_{11}$ H_2CO absorption toward the "Orion-S" region. These $1_{10} \rightarrow 1_{11}$ and $5_{14} \rightarrow 5_{15}$ emission measurements have been combined with 6" resolution measurements of the $2_{11} \rightarrow 2_{12}$ transition of H_2CO (Mangum et al. 1990) in a spherical large velocity gradient model of the H_2CO excitation to derive the H_2 density and H_2CO column density in the hot core, compact ridge, and northern cloud. Typical peak densities lie in the range (3–8) × 10^5 cm^{-3}, with H_2CO column densities in the range 10^{16}–10^{17} cm^{-2}. Highest spatial densities but lowest column densities occur in the northern cloud, while lowest spatial densities but highest column densities characterize the compact ridge. A critical discussion of H_2CO as a spatial density probe demonstrates that the *K*-doublet transitions provide an excellent spatial density probe, attaining substantial optical depths only at the highest column densities.

Subject headings: ISM: individual objects (Orion Nebula) — ISM: molecules

1. INTRODUCTION

At a distance of 480 ± 80 pc (Genzel et al. 1981), the Orion-KL, or OMC-1, molecular cloud is the prototypical high-mass star-forming region. On arcminute size scales, Orion-KL is composed of a dense, quiescent "ridge" of cool gas running southwest ($V_{LSR} \simeq 8$ km s^{-1}) to northeast ($V_{LSR} \simeq 10$ km s^{-1}). Near the center of this ridge and located ~1' to the northwest of the Trapezium cluster is the Kleinmann & Low (1967) nebula, the brightest component of infrared emission in the region. Buried deep within this nebula is a tight ($\lesssim 10^4$ AU) group of young, massive stars, the brightest of which is IRc2. Most of the 10^5 $L_\odot$ of bolometric luminosity received from the Kleinmann-Low nebula (Werner et al. 1976) is supplied by IRc2 (Wynn-Williams et al. 1984).

The molecular emission from the Orion-KL region is comprised of at least four subsources. Some of these subsources may relate to interaction between IRc2 and the dense gas in the ridge, while others may locate independent star-forming events. Turbulent gas, thought to be physically associated with an outflow of material from IRc2, is observed as high-velocity wings ($\Delta v \gtrsim 18$ km s^{-1}) on CO (Wilson, Jefferts, & Penzias 1970; Thaddeus et al. 1972; Zuckerman, Kuiper, & Rodriguez-Kuiper 1976), SiO (Wright et al. 1983), H_2CO (Wootten & Loren 1984), HCO^+ (Vogel et al. 1985), SO (Plambeck et al. 1982), and SO_2 (Plambeck & Wright 1988a) emission profiles and maps. This "plateau" or "pedestal" emission, first of the subsources, is actually composed of two components; a high-velocity ($\Delta v \gtrsim 30$ km s^{-1}) outflow centered near IRc2 which appears to be bipolar and oriented along a southeast-northwest position angle of ~120° (Wright et al 1983; Vogel et al. 1985; Masson et al. 1987), and a low-velocity ($\Delta v \simeq 18$ km s^{-1}; Genzel et al. 1981) outflow centered on IRc2 and best characterized by the "doughnut" of SO emission observed by Plambeck et al. (1982). As shown by the proper motions of the H_2O masers (Genzel et al. 1981), this low-velocity outflow is expanding away from IRc2 and appears to have compressed much of the molecular material in the region into spectrally identifiable components.

The second subsource is the "hot core," a clump of hot, dense material situated ~2" south of IRc2. Identifiable by its characteristic velocity ($V_{LSR} \simeq 6$ km s^{-1}), large line width ($\Delta v \gtrsim 10$ km s^{-1}) and high kinetic temperature ($T_K \simeq$ 150–300 K), the hot core may locate dense clumps left over from the formation of IRc2. Located ~10" southwest of IRc2 lies a third subsource, the southern velocity component ($V_{LSR} \simeq 8$ km s^{-1}) of the Orion-KL ridge, known as the "compact ridge" (also called the "condensed ridge," "southern condensation," or "spike"). Characterized by a moderate line width ($\Delta v \simeq 4$ km s^{-1}) and kinetic temperature ($T_K \simeq 100$ K), the compact ridge is observed to be a dense condensation of material ~25" (~0.06 pc) in size which may harbor young massive stars (Mangum et al. 1990). The fourth

[1] Postal address.
[2] The National Radio Astronomy Observatory is operated by Associated Universities, Inc., under cooperative agreement with the National Science Foundation.

subsource is the northern velocity component ($V_{LSR} \simeq 10$ km s^{-1}) of the ridge, known as the "northern" or "10 km s^{-1} feature." This northern cloud is a cool ($T_K \simeq 50$ K) quiescent ($\Delta v \simeq 1.5$ km s^{-1}) condensation located $\sim 15''$ northwest of IRc2. The northern cloud is the most dynamically quiescent of the four Orion-KL subsources, but does appear to be interacting with the low-velocity outflow of the plateau emission component (Plambeck et al. 1982; Plambeck & Wright 1988b; Mangum et al. 1990).

Broad-band spectral surveys of Orion-KL (Johansson et al. 1984; Sutton et al. 1985; Blake et al. 1986, 1987; Jewell et al. 1989; Turner 1989) have detailed the striking chemical diversity of the four distinct subsources in this region. These surveys suggest that the formaldehyde (H_2CO) molecule provides one of the most effective probes of the character of these clumps. Its high abundance and relative chemical homogeneity in the Orion-KL subsources makes it a reliable and unbiased probe of these regions. By utilizing the unique emission properties of the "*K*-doublet" transitions of H_2CO, we have applied a non-LTE excitation model, constrained by interferometric measurements of three of these transitions, to the hot core, compact ridge, and northern cloud subsources. This analysis has led to good estimates of the spatial density and H_2CO column density in these sources and has shown how the *K*-doublet transitions of H_2CO can be used as sensitive probes of the spatial density in star-forming regions.

The spatial resolutions of line surveys or of previous multi-transition analyses ($\theta_B \gtrsim 30'' = 0.07$ pc $= 14{,}000$ AU) of Orion-KL have been insufficient to detail the spatial and dynamical relationships between emission components clustered within the central 0.05 pc region. The multitransition study at 2400 AU resolution presented here clearly separates these regions and allows us to determine the individual characteristics and the relationships between these star-forming clumps.

2. OBSERVATIONS

2.1. $1_{10} \rightarrow 1_{11}$ H_2CO

The $1_{10} \rightarrow 1_{11}$ transition of H_2CO was observed on 1989 September 5 using the NRAO Very Large Array. The 27 operational antennas were in the C configuration during these observations, which yielded projected antenna spacings ranging from 1.1 to 55 kλ. The total observing bandwidth of 1.563 MHz was sampled by 128 spectral channels in each of two orthogonally polarized IFs which, after on-line Hanning smoothing, resulted in a frequency resolution and channel spacing of 12.207 kHz. At the line rest frequency of 4.8296639 GHz centered at an LSR velocity of 9.0 km s^{-1}, this channel spacing afforded a velocity resolution of 0.76 km s^{-1} and a total velocity coverage of $-39.5 \leq V_{LSR} \leq 56.8$ km s^{-1}. Orion-KL was observed at an antenna pointing and phase center position of $\alpha(1950) = 05^h32^m47^s.0$, $\delta(1950) = -05°24'26''$. The basic observing sequence consisted of 30 minute observations of Orion-KL each followed by a 10 minute observation of the phase calibration source 0528+134 (measured flux 2.1 Jy). To establish the flux density scale, one 10 minute observation of 3C 48 (assumed flux 5.42 Jy) was made. The accuracy of the flux density calibration is $\sim 5\%$. A 10 minute observation of the source 3C 84 (measured flux 40.3 Jy) was used to calibrate the bandpass in each IF.

Bad visibilities were flagged and the antenna amplitudes and phases were calibrated within AIPS. After calibrating each IF, the two $u-v$ data sets were combined to increase the overall sensitivity of the observations. Maps of each spectral line channel were made using a cell size of 1'' with natural weighting and no tapering of the $u-v$ data. The resulting synthesized beam size was $5''.9 \times 4''.4$, position angle $-8°.4$. Based on the observed single antenna line width, a total of 70 channels were assumed to be devoid of emission and absorption. These line-free channels were averaged to form a line-free continuum map which was subtracted from the channel maps. After this dirty map continuum subtraction, each spectral line channel which contained emission or absorption was CLEANed in the usual manner. A total of nine channels over the LSR velocity range of 3.7–10.5 km s^{-1} were found to contain $1_{10} \rightarrow 1_{11}$ H_2CO emission or absorption. Since the primary beam in these observations ($9'.3$) is much larger than the distance between the pointing center and the most widely separated emission or absorption feature ($\sim 2'$), we have not corrected for the response of the primary beam. The rms noise in these CLEANed maps was found to be 2.2 mJy beam^{-1}, which corresponds to a main beam brightness temperature of 4.5 K (K/Jy = 2028).

2.2. $5_{14} \rightarrow 5_{15}$ H_2CO

Data were obtained at eight configurations of the three-element BIMA array[3] at the Hat Creek Radio Observatory between 1988 December and 1989 October. Projected antenna spacings at the observed H_2CO $5_{14} \rightarrow 5_{15}$ transition rest frequency of 72.409092 GHz ranged from 1.4 to 29 kλ. At 72 GHz, the three 6.1 m diameter antennas have primary beamwidths of $\sim 2'.7$. The phase tracking center was $\alpha(1950) = 05^h32^m47^s.0$, $\delta(1950) = -05°24'21''$, approximately 3'' north of IRc2. The quasars 0420−014 and 0528+134 were used as phase calibrators. Phase structure within the IF passband was calibrated from observations of 3C 273 each day. The amplitude scale was referenced to 0420−014; its 72 GHz flux density, measured from time to time by comparison with planets, was 4.8 ± 0.3 Jy over the course of the observations. The uncertainty in our absolute flux scale is estimated to be 15%. With the receivers tuned to their lower frequency limit, the single sideband system temperatures were 500–900 K, scaled to outside the atmosphere.

Spectra were obtained with a digital cross-correlation spectrometer, configured to give a velocity resolution of 0.32 km s^{-1} over an 80 km s^{-1} wide velocity range. To increase signal-to-noise, the data were smoothed to a velocity resolution of 0.65 km s^{-1}. The data were mapped and CLEANed using the RALINT data reduction package developed at U.C. Berkeley. The synthesized beamwidth was $7''.9 \times 7''.4$ with the visibility data uniformly weighted and the rms noise was 0.625 Jy beam^{-1} (2.5 K) in individual 0.65 km s^{-1} wide velocity channels.

3. RESULTS

3.1. $1_{10} \rightarrow 1_{11}$ H_2CO

Figure 1 presents the individual channel maps with detected H_2CO $1_{10} \rightarrow 1_{11}$ emission and absorption. The rms noise in each of these maps is 2.2 mJy beam^{-1} (4.5 K). Figure 2 is the total velocity-integrated emission and absorption. As Figures 1 and 2 demonstrate, the general structure is that of a compact

[3] Operated by the University of California at Berkeley, the University of Illinois, and the University of Maryland, with support from the National Science Foundation.

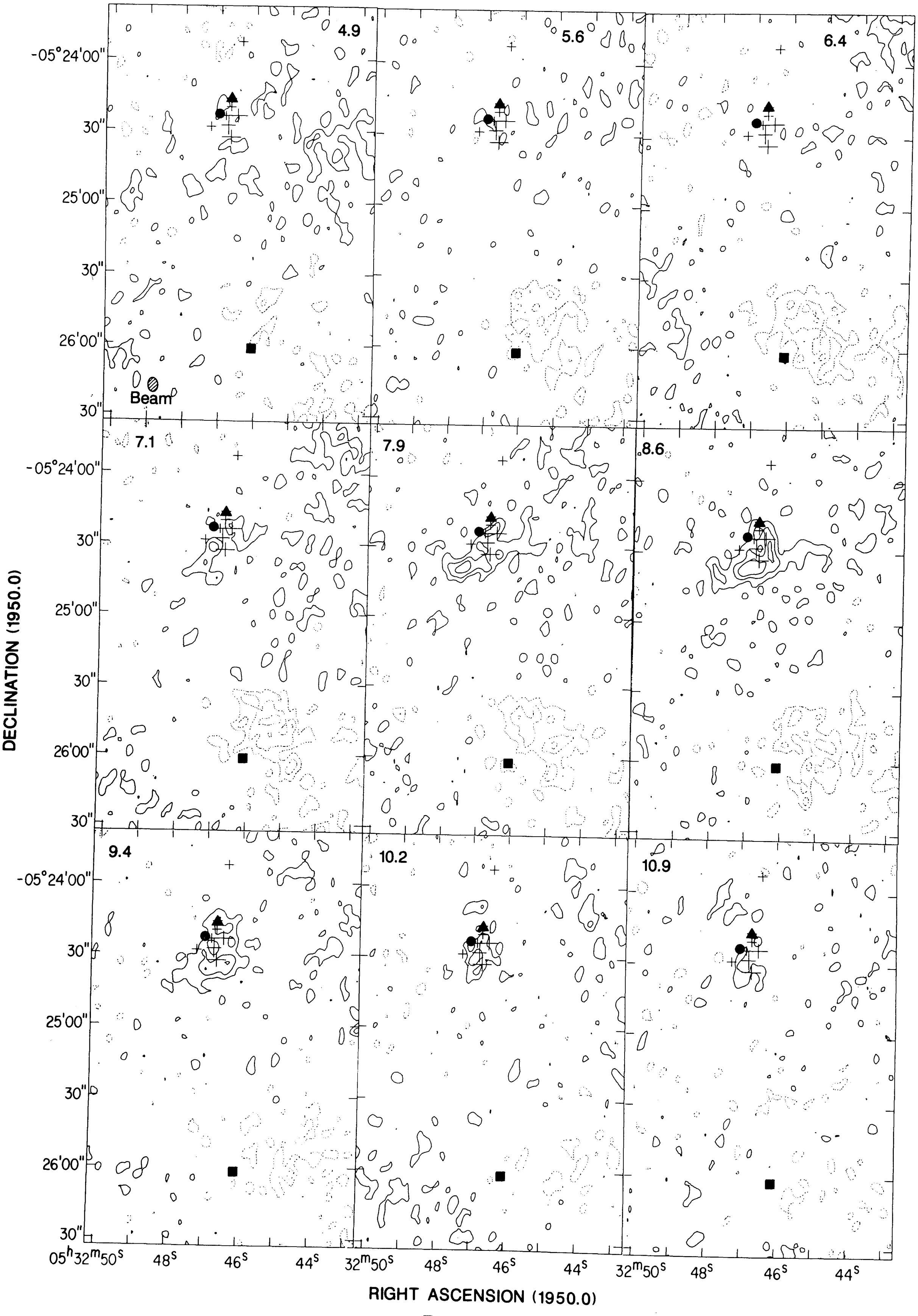
4.9
5.6
6.4
7.1
7.9
8.6
9.4
10.2
10.9
Beam
-05°24'00"
30"
25'00"
30"
26'00"
30"
DECLINATION (1950.0)
05h32m50s
48s
46s
44s
32m50s
RIGHT ASCENSION (1950.0)

FIG. 1

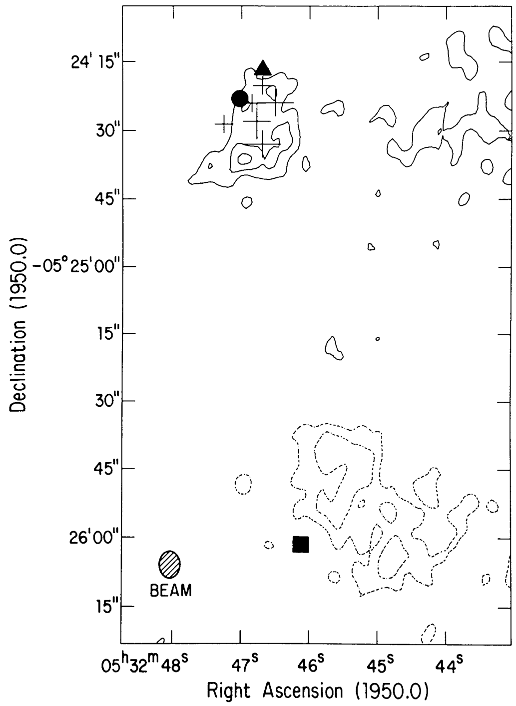

FIG. 2.—Total integrated $1_{10} \rightarrow 1_{11}$ H_2CO emission and absorption from Orion-KL. The contours are −40, −25, 25, 40, and 55 mJy beam^{-1} km s^{-1} (−80, −50, 50, 80, and 110 K km s^{-1}). The positions of the infrared and millimeter continuum sources and the synthesized beam are shown as in Fig. 1.

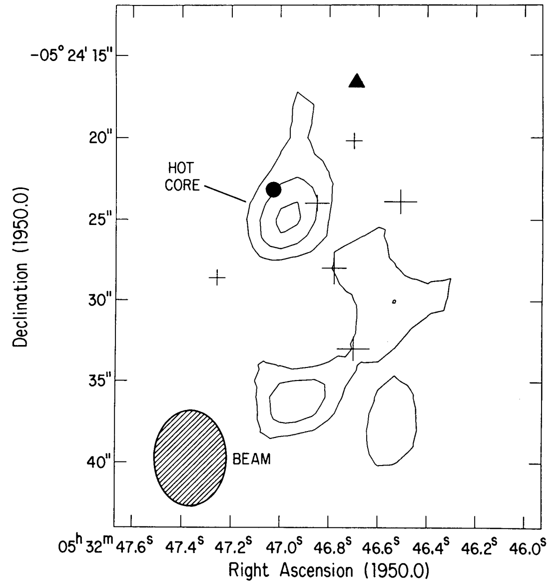

FIG. 3.—Integrated $1_{10} \rightarrow 1_{11}$ H_2CO emission from the hot core. The velocity ranges for the integration are $2.9 < V_{LSR} < 6.7$ km s^{-1} and $9.0 < V_{LSR} < 12.1$ km s^{-1}. The contours are 15, 20, and 25 mJy beam^{-1} km s^{-1} (30, 40, and 50 K km s^{-1}). The positions of the infrared sources and the synthesized beam are shown as in Fig. 1. The H_2CO hot core is located ~2" southwest of IRc2.

emission region to the northeast with an extended broad-lined absorption component located to the southwest. This structure was also observed in the 16" resolution H_2CO $1_{10} \rightarrow 1_{11}$ observations of Johnston et al. (1983). The observed emission region is spatially coincident with the H_2CO $2_{11} \rightarrow 2_{12}$ (Mangum et al. 1990) and $5_{14} \rightarrow 5_{15}$ (§ 3.2) emission distributions. To estimate how much of the single antenna flux we have recovered in both emission and absorption, we compare our measured total integrated intensities with the 2'.6 resolution measurements of Zuckerman, Palmer, & Rickard (1975). Integrating over all channels with emission and over the emission region source extent (≃25") we measure a total integrated emission intensity of 43.3 K km s^{-1}. Doing the same for the absorption component ($\theta_S \simeq 28''$), we measure −45.7 km s^{-1}. From Zuckerman et al. (1975) we estimate an integrated emission intensity of ~53 K km s^{-1} and an integrated absorption intensity of ~ −50 K km s^{-1}. Therefore, our interferometer observations recover nearly all of the emission and absorption intensity measured by a single antenna.

By integrating over the appropriate velocity ranges, we have separated the hot core, compact ridge, and northern cloud emission components. In the following we analyze the properties of these emission regions as derived from their $1_{10} \rightarrow 1_{11}$ emission.

3.1.1. *Hot Core*

It is apparent from Figure 1 that there is very little emission observed near the characteristic hot core velocity of 6 km s^{-1}. Therefore, in order to delineate any low-level hot core emission, we have constructed an integrated intensity map. Because the H_2CO hot core and compact ridge components are partially blended both spatially and in velocity, we have summed the integrated emission over a low ($2.9 < V_{LSR} < 6.7$ km s^{-1}) and high ($9.0 < V_{LSR} < 12.1$ km s^{-1}) velocity range (which excludes the most intense emission from the compact ridge) in order to delineate any low-level hot core emission. Figure 3 is the integrated emission over these velocity ranges. The emission peak in Figure 3 is located ~2" southwest of IRc2 and is coincident with the H_2CO $2_{11} \rightarrow 2_{12}$ hot core (Mangum et al. 1990), leading us to believe that we have detected the hot core in the $1_{10} \rightarrow 1_{11}$ transition. The upper state energy of the $1_{10} \rightarrow 1_{11}$ transition is only 15.4 K above the ground state, where the molecular state populations will be low in a warm gas. Given the high kinetic temperature observed toward the hot core ($T_K \simeq 150$–300 K), it is not surprising that $1_{10} \rightarrow 1_{11}$ emission is weak in this source. Table 1 lists the measured $1_{10} \rightarrow 1_{11}$ emission properties for this source. Note that the hot core position and size are measured from the hot core integrated intensity map (Fig. 3) while the integrated intensity is measured from the total integrated intensity map (Fig. 2).

3.1.2. *Compact Ridge*

As was the case in the H_2CO $2_{11} \rightarrow 2_{12}$ measurements (Mangum et al. 1990), the compact ridge feature is the most dominant emission component in our $1_{10} \rightarrow 1_{11}$ observations. Shown in Figure 4 is the integrated emission over the H_2CO $1_{10} \rightarrow 1_{11}$ compact ridge ($6.0 < V_{LSR} < 9.8$ km s^{-1}). The structure of the H_2CO $1_{10} \rightarrow 1_{11}$ compact ridge emission is the

FIG. 1.—Channel maps of the $1_{10} \rightarrow 1_{11}$ H_2CO emission toward Orion-KL. The contours are −13.2, −8.8, −4.4, 4.4, 8.8, and 13.2 mJy beam^{-1} (−26.8, −17.8, −8.9, 8.9, 17.8, and 26.8 K). The central LSR velocity is given for each channel. The 5".9 × 4".4 synthesized beam is shown in the first channel. The positions of the infrared sources IRc1 through IRc9 (Downes et al. 1981) are indicated. The filled circle is IRc2 and the filled triangle is IRc1 (the Becklin-Neugebauer object). A filled square designates the position of the 3.2 mm continuum source CS 3 (Mundy et al. 1986).

TABLE 1

$1_{10} \rightarrow 1_{11}$ H_2CO COMPONENT PROPERTIES

Component	α(1950)	δ(1950)	$\theta_{max} \times \theta_{min}$	Position Angle	Peak T_B (K)	FWZI (km s^{-1})	$\int T_B dV$ (K km s^{-1})
Hot core	05^{h}32^{m}46^s.9	−05°24′24″	10″.9 × 7″.0	16°	<9.0[a]	9.2	84.8[b]
Compact ridge	05 32 46.8	−05 24 33	34.7 × 20.4	135	40.5	3.8	86.9
Northern cloud	05 32 47.5	−05 24 08	~15 × 10	~45	10.2	3.1	28.1
Orion-S	05 32 45.4	−05 25 48	35.5 × 22.2	29	−30.9	6.1	−107.6

[a] Upper limit given as twice the rms noise in a channel map.
[b] May include some emission from the compact ridge component.

same as that observed in the $2_{11} \rightarrow 2_{12}$ measurements (Mangum et al. 1990). There is an elongated peak of size ~15″ × 10″ which is inclined along a northwest-southeast position angle. Located less than 5″ (2300 AU) to the northwest of the H_2CO integrated emission peak is IRc5, a moderately strong 20 μm continuum source which may be an object in an early stage of protostellar evolution (Downes et al. 1981; Wynn-Williams et al. 1984). There is also a strong compact source of centimeter-wavelength continuum emission located less than 5″ from the H_2CO emission peak (Churchwell et al. 1987) whose radio spectral characteristics are indicative of a B3 ZAMS star. Both of these observations suggest that the compact ridge is actively forming stars. Measurements of the $1_{10} \rightarrow 1_{11}$ compact ridge emission properties are given in Table 1.

3.1.3. *Northern Cloud*

Located ~15″ to the northeast of the hot core and compact ridge there is a weak, narrow-lined condensation detected in the $1_{10} \rightarrow 1_{11}$ maps. Due to its FWZI (3.1 km s^{-1}), V_{LSR} (10.5 km s^{-1}), and spatial coincidence with similar features detected in the $2_{11} \rightarrow 2_{12}$ (Mangum et al. 1990) and $5_{14} \rightarrow 5_{15}$ (§ 3.2) transitions of H_2CO, we identify this condensation as the northern cloud (Fig. 5). Like the $2_{11} \rightarrow 2_{12}$ northern cloud emission, the $1_{10} \rightarrow 1_{11}$ emission appears to be composed of two intensity peaks situated along a northeast-southwest position angle. The measured $1_{10} \rightarrow 1_{11}$ emission characteristics for this component are given in Table 1.

3.1.4. $1_{10} \rightarrow 1_{11}$ *Absorption*

Situated ~75″ southwest of the $1_{10} \rightarrow 1_{11}$ emission region there is a source of $1_{10} \leftarrow 1_{11}$ H_2CO *absorption* over the velocity range 3.7–9.8 km s^{-1} (see Figs. 1 and 2). This condensation has been detected previously in the 16″ resolution H_2CO $1_{10} \rightarrow 1_{11}$ observations of Johnston et al. (1983), in 400 μm (Keene, Hildebrand, & Whitcomb 1982) and 3.2 mm (Mundy et al. 1986) dust continuum emission, as well as NH_3 (1, 1) and (2, 2) (Batrla et al. 1983), $C^{18}O$ $J = 1 \rightarrow 0$ (Wilson et al. 1986), and H_2CO $4_{13} \rightarrow 3_{12}$ (Mangum et al. 1990) emission. This $1_{10} \leftarrow 1_{11}$ absorption component is also associated with CS $J = 2 \rightarrow 1$ (Mundy et al. 1988), $2_{11} \rightarrow 2_{12}$ H_2CO (Bastien et al. 1985), SiO $J = 2 \rightarrow 1$ and $5 \rightarrow 4$, $C^{34}S$ $J = 2 \rightarrow 1$, $3 \rightarrow 2$, and $5 \rightarrow 4$, and CH_3CN $J = 5 \rightarrow 4$ and $13 \rightarrow 12$ (Ziurys, Wilson, & Mauersberger 1990) emission. Ziurys et al. have also detected a

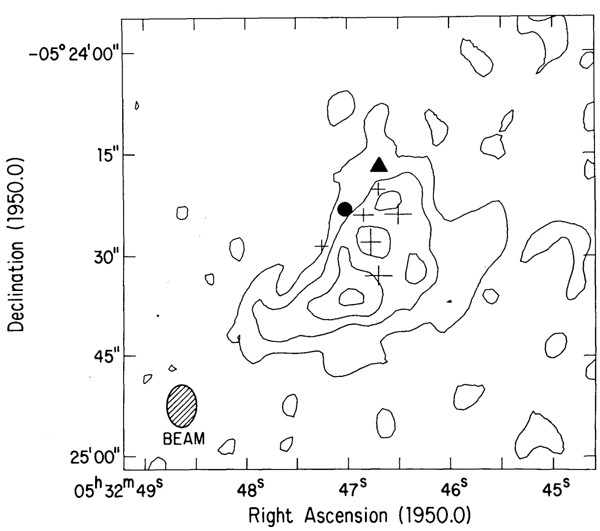

FIG. 4.—Integrated $1_{10} \rightarrow 1_{11}$ H_2CO emission from the compact ridge. The velocity range for the integration is $6.0 < V_{LSR} < 9.8$ km s^{-1}. The contours are 10, 20, 30, and 40 mJy beam^{-1} km s^{-1} (20, 40, 60, and 80 K km s^{-1}). The positions of the infrared sources and the synthesized beam are shown as in Fig. 1.

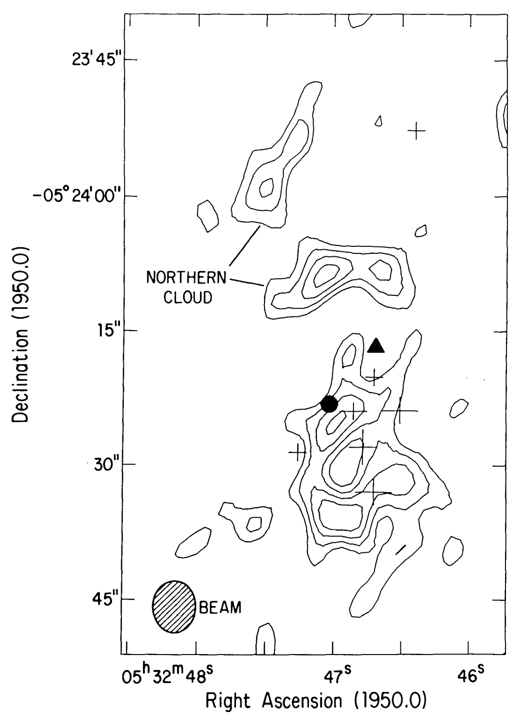

FIG. 5.—Integrated $1_{10} \rightarrow 1_{11}$ H_2CO emission from the northern cloud. The velocity range for the integration is $9.0 < V_{LSR} < 12.1$ km s^{-1}. The contours are 5.0, 7.5, 10.0, and 12.5 mJy beam^{-1} km s^{-1} (10, 15, 20, and 25 K km s^{-1}). The positions of the infrared sources and the synthesized beam are shown as in Fig. 1. The two components of the northern cloud are also indicated.

small bipolar outflow, directed along a north-south position angle, in their SiO emission maps. Table 1 lists the measured physical properties for this component (we have adopted the notation of Ziurys et al. and call this source Orion-S).

Comparison with the emission distributions listed above indicates that the NH_3 and $C^{18}O$ emission regions are coincident with the $1_{10} \leftarrow 1_{11}$ absorption while the CS, $2_{11} \rightarrow 2_{12}$ H_2CO, SiO, $C^{34}S$, and CH_3CN emission are located $\sim 15''$ to the south of the $1_{10} \leftarrow 1_{11}$ absorption. The high observed $1_{10} \leftarrow 1_{11}$ brightness temperature (-30.9 K) indicates that the gas which gives rise to this absorption is probably situated in front of or inside the southwestern edge of the H II region (Wilson & Pauls 1984; Johnston et al. 1983). Therefore, it is likely that the $1_{10} \leftarrow 1_{11}$ absorption occurs in a lower density region just to the north of the millimeter continuum, CS, $2_{11} \rightarrow 2_{12}$ H_2CO, SiO, $C^{34}S$, and CH_3CN emission peaks, where the centimeter continuum is still strong. In our line-free 6 cm continuum map there is an ~ 60 mJy beam^{-1} peak in the emission located at the position of Orion-S, consistent with this interpretation.

3.2. $5_{14} \rightarrow 5_{15}$ H_2CO

We present in Figure 6 the H_2CO $5_{14} \rightarrow 5_{15}$ channel maps. The rms noise in each of these maps is 0.625 Jy beam^{-1} (2.5 K). Note that in these emission maps there is a small contribution due to continuum emission which has not been subtracted (see Mangum, Plambeck, & Wootten 1991). In Figure 7 we show the total integrated emission map. To estimate how much of the single antenna $5_{14} \rightarrow 5_{15}$ flux we have recovered, we compare our measured total integrated intensity with the 1′.6 resolution measurements of Greason (1986). Integrating over all channels with emission and over the emission region source extent ($\simeq 42''$), the total integrated emission intensity is ~ 28 K km s^{-1}. From Greason (1986), we estimate an integrated emission intensity of ~ 29 K km s^{-1}. Therefore, our interferometer observations recover essentially all of the integrated emission intensity measured by a single antenna. Comparison with the H_2CO $1_{10} \rightarrow 1_{11}$ (see § 3.1) and $2_{11} \rightarrow 2_{12}$ (Mangum et al. 1990) channel maps reveals many similarities between the three K-doublet transitions. Because the upper state energy of the $5_{14} \rightarrow 5_{15}$ transition is 65.9 K, the highest of the observed K-doublet transitions, it traces higher excitation regions. Therefore, one would expect to observe an increased contribution to the Orion-KL H_2CO $5_{14} \rightarrow 5_{15}$ emission from the hot core over the contribution measured in the $1_{10} \rightarrow 1_{11}$ transition.

As was done in § 3.1, we have integrated over specific velocity ranges in order to delineate the hot core, compact ridge, and northern cloud components and discuss each of these regions below.

3.2.1. *Hot Core*

To circumvent the spatial and spectral blending of the H_2CO hot core and compact ridge components, we have summed the integrated emission over $1.1 < V_{LSR} < 6.3$ and $9.5 < V_{LSR} < 11.5$ km s^{-1} to delineate the $5_{14} \rightarrow 5_{15}$ H_2CO emission from the hot core (Fig. 8). Due to its greater sensitivity to warmer gas, the $5_{14} \rightarrow 5_{15}$ transition gives us a better representation of the hot core than the $1_{10} \rightarrow 1_{11}$ transition

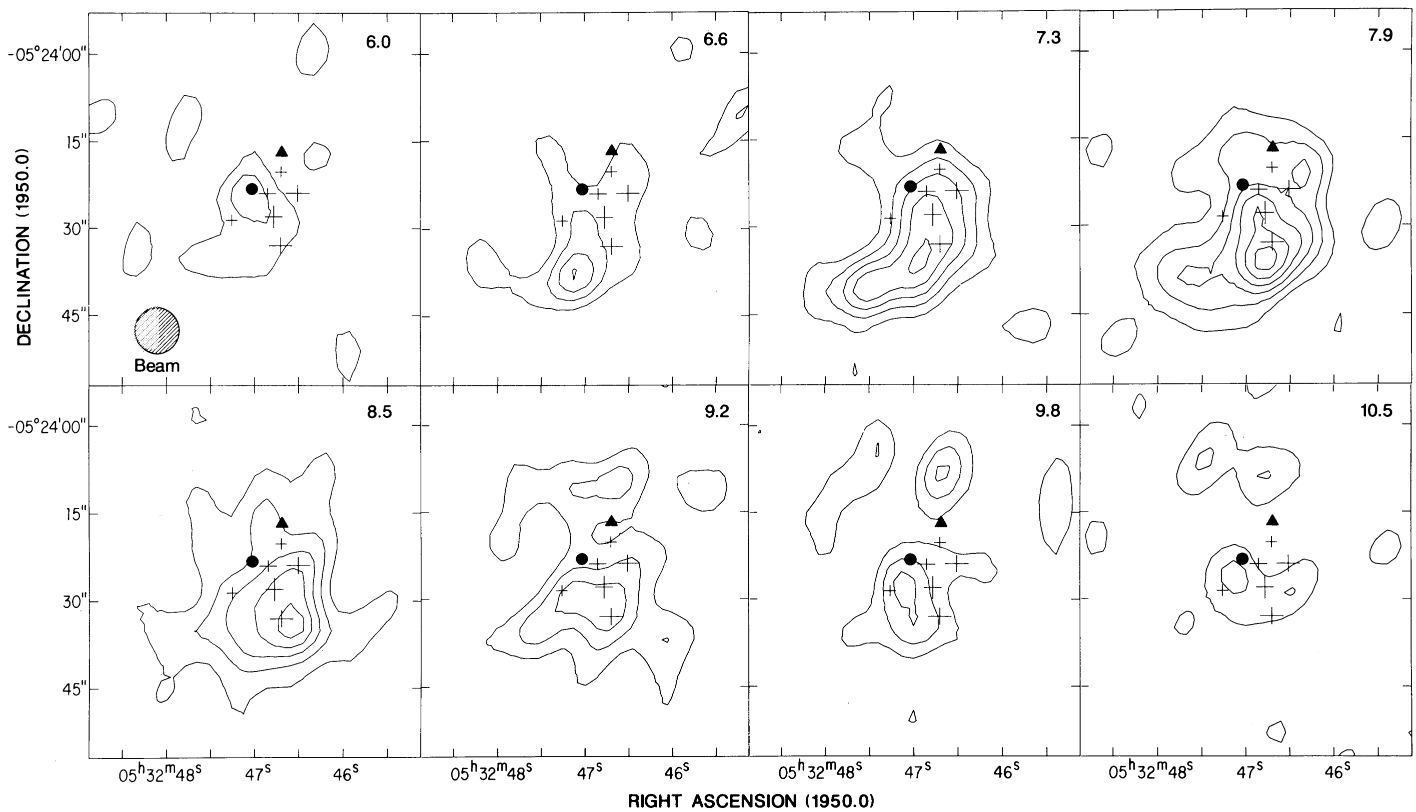

FIG. 6.—Channel maps of the $5_{14} \rightarrow 5_{15}$ H_2CO emission toward Orion-KL. The contours are 1.25, 2.5, 3.75, 5.0, 6.25, and 7.5 Jy beam^{-1} (5, 10, 15, 20, 25, and 30 K). The central LSR velocity is given in the upper right-hand corner of each channel. The 7″.9 × 7″.4 synthesized beam is shown in the first channel. The positions of the infrared sources are indicated as in Fig. 1.

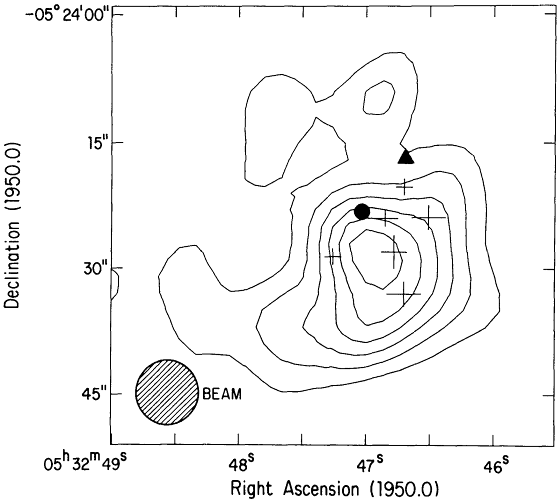

FIG. 7.—Total integrated $5_{14} \rightarrow 5_{15}$ H_2CO emission from Orion-KL. The contours are 6, 10, 14, 18, 22, and 26 Jy beam^{-1} km s^{-1} (24, 40, 56, 72, 88, and 104 K km s^{-1}). The positions of the infrared sources are indicated as in Fig. 1, while the synthesized beam is shown in the lower left-hand corner.

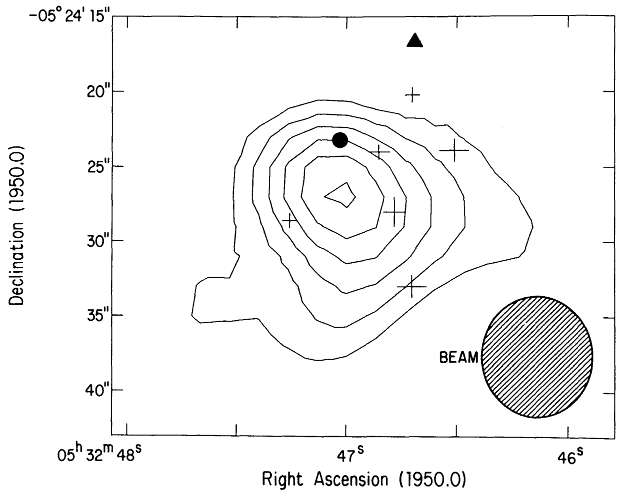

FIG. 8.—Integrated $5_{14} \rightarrow 5_{15}$ H_2CO emission from the hot core. The velocity range for the integration is $1.1 < V_{LSR} < 6.3$ km s^{-1} and $9.5 < V_{LSR} < 11.5$ km s^{-1}. The contours are 5, 7, 9, 11, 13, and 15 Jy beam^{-1} km s^{-1} (20, 28, 36, 44, 52, and 60 K km s^{-1}). The positions of the infrared sources are shown as in Fig. 1, and the synthesized beam is shown as in Fig. 6.

(see § 3.1.1 and Fig. 3). The increasing dominance of the hot core component in the higher excitation H_2CO emission is apparent in our measured integrated intensities. In the $5_{14} \rightarrow 5_{15}$ transition, the hot core integrated intensity is ~26% larger than the integrated intensity from the compact ridge (see Table 2), while the integrated intensities are comparable in the $2_{11} \rightarrow 2_{12}$ (Mangum et al. 1990) and $1_{10} \rightarrow 1_{11}$ (Table 1) transitions. Clearly, our K-doublet measurements support the character of the Orion-KL hot core—a dense, hot gas condensation near the outflow source IRc2.

3.2.2. *Compact Ridge*

The compact ridge is the largest and brightest of the three emission regions. In Figure 9 we show the $5_{14} \rightarrow 5_{15}$ integrated emission from the compact ridge ($5.7 < V_{LSR} < 10.2$ km s^{-1}). The overall structure of the $5_{14} \rightarrow 5_{15}$ H_2CO compact ridge is the same as that observed in the $1_{10} \rightarrow 1_{11}$ (§ 3.1.2) and $2_{11} \rightarrow 2_{12}$ (Mangum et al. 1990) transitions. In detail, though, the $2_{11} \rightarrow 2_{12}$ and $5_{14} \rightarrow 5_{15}$ transitions appear to be more strongly peaked toward IRc5 than the $1_{10} \rightarrow 1_{11}$ transition, which extends more to the southeast (see Fig. 10). This may be due to the effect of an increasing temperature or density gradient from the southeast to the northwest, toward IRc5. The decreasing excitation with distance from IRc5 suggests that it locates a distinct energy source, in accord with the suggestion by Downes et al. (1981) and Wynn-Williams et al. (1984) that IRc5 may be an embedded protostar. We will investigate this apparent gradient in § 4.2.2. Table 2 lists the measured H_2CO $5_{14} \rightarrow 5_{15}$ properties for this component.

3.2.3. *Northern Cloud*

The weakest component of the H_2CO $5_{14} \rightarrow 5_{15}$ emission in Orion-KL originates from the dense ridge condensation located ~15" northeast of IRc2. Unlike the two-component structure observed in the $1_{10} \rightarrow 1_{11}$ and $2_{11} \rightarrow 2_{12}$ transitions, the $5_{14} \rightarrow 5_{15}$ emission originates only from the southwestern component of this source. Figure 11 represents the integrated intensity from the H_2CO $5_{14} \rightarrow 5_{15}$ emission at the northern cloud ($9.5 < V_{LSR} < 11.4$ km s^{-1}). Since there is a cluster of H_2O masers located along the southwestern periphery of the northern cloud (Genzel et al. 1981), the outflow from IRc2 appears to impact the dense northern cloud condensation. This would heat the southwestern portion of the northern cloud and produce a density and/or temperature gradient along its length, causing the higher-excitation $5_{14} \rightarrow 5_{15}$ transition to appear only on the southwestern portion of this source. In Table 2 we give the measured properties of the northern cloud $5_{14} \rightarrow 5_{15}$ H_2CO emission.

4. ANALYSIS

4.1. H_2CO *as a Probe*

H_2CO is a proven tracer of the high-density environs of molecular clouds. It is ubiquitous: H_2CO is associated with

TABLE 2
$5_{14} \rightarrow 5_{15}$ H_2CO COMPONENT PROPERTIES

Component	α(1950)	δ(1950)	$\theta_{max} \times \theta_{min}$	Position Angle	Peak T_B (K)	FWZI (km s^{-1})	$\int T_B dV$[a] (K km s^{-1})
Hot core	05h32m47.0s	−05°24'28"	14".9 × 12".4	118°	14.4	10.4	99.7
Compact ridge	05 32 46.9	−05 24 31	25.6 × 16.2	144	32.4	4.5	78.9
Northern cloud	05 32 47.6	−05 24 09	20.4 × 7.2	131	11.0	1.9	18.1

[a] 16.6, 3.6, and 1.1 K km s^{-1} have been subtracted from the hot core, compact ridge, and northern cloud measured integrated intensities, respectively, to compensate for the contribution to the emission due to dust continuum toward these components.

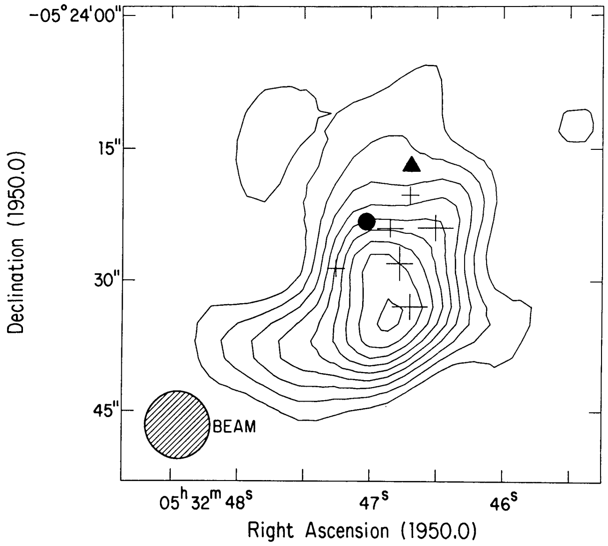

FIG. 9.—Integrated $5_{14} \rightarrow 5_{15}$ H_2CO emission from the compact ridge. The velocity range for the integration is $5.7 < V_{LSR} < 10.2$ km s^{-1}. The contours are 4, 6, 8, 10, 12, 14, 16, 18, and 20 Jy $beam^{-1}$ km s^{-1} km s^{-1} (16, 24, 32, 40, 48, 56, 64, 72, and 80 K km s^{-1}). The positions of the infrared sources are shown as in Fig. 1, and the synthesized beam is shown as in Fig. 6.

80% of the H II regions surveyed by Downes et al. (1980), and possesses a large number of observationally accessible transitions from centimeter to far-infrared wavelengths. Because H_2CO is a slightly asymmetric rotor molecule, each rotational level is split by this asymmetry into two energy levels. Therefore, the energy levels must be designated by a total angular momentum quantum number, J, the projection of J along the symmetry axis for a limiting prolate symmetric top, K_{-1}, and the projection of J along the symmetry axis for a limiting oblate symmetric top, K_{+1}. This splitting leads to three basic types of transition: the high-frequency $\Delta J = \mp 1$, $\Delta K_{-1} = 0$, $\Delta K_{+1} = \mp 1$ "P-branch" and "R-branch" transitions and the lower frequency $\Delta J = 0$, $\Delta K_{-1} = 0$, $\Delta K_{+1} = \pm 1$ "Q-branch" transitions, popularly known as the "K-doublet" transitions. The P-branch transitions are only seen in emission in regions where $n(H_2) \gtrsim 10^5$ cm^{-3}. The excitation of the K-doublet transitions, though, is not so simple. For $n(H_2) \lesssim 10^5$ cm^{-3}, the lower energy states of the $1_{10} \rightarrow 1_{11}$ and $2_{11} \rightarrow 2_{12}$ K-doublet transitions become overpopulated due to a collisional selection effect (Evans et al. 1975; Garrison et al. 1975). This overpopulation cools the $J = 1$ and 2 K-doublets to an excitation temperature lower than that of the cosmic microwave background, causing them to appear in absorption. For $n(H_2) \gtrsim 10^5$ cm^{-3}, this collisional pump is quenched and the $J = 1$ and 2 K-doublets are then seen in emission. The exact density at which these K-doublets go into emission is a function of the H_2CO abundance and gas kinetic temperature.

Does this anomalous excitation occur in the higher ($J \geq 3$) K-doublet transitions? In the statistical equilibrium models of Evans et al. (1975) and in the quantum mechanical calculations of Garrison et al. (1975), $T_{ex}(1_{10} \leftarrow 1_{11}) < T_{ex}(2_{11} \leftarrow 2_{12})$ over the entire range in density where these transitions are in absorption. Evans et al. and Garrison et al. also found that the $1_{10} \leftarrow 1_{11}$ transition stays in absorption over a slightly larger range in density than the $2_{11} \leftarrow 2_{12}$ transition. This is primarily due to the fact that the density required to excite the $2_{11} \leftarrow 2_{12}$ transition (often referred to as the "critical density") is larger than that of the $1_{10} \leftarrow 1_{11}$ transition. Assuming that this behavior is also exhibited by the $J \geq 3$ K-doublets, one would expect to observe progressively weaker absorption and a progressively narrower range in density over which this absorption is observed as one measures higher excitation K-doublets. At some point in this progression, the K-doublets will no longer appear in absorption and will only be seen in emission.

To verify that indeed this excitation behavior of the K-doublet transitions does occur, we have compared the K-doublet radiation temperatures predicted by our non-LTE excitation models (see § 4.2) over a range in kinetic temperature, density, and abundance in which the $J = 1$ and 2 K-doublets are in absorption. As expected, our models do replicate the excitation behavior described above. For $T_K = 100$ K, $n(H_2) = 10^5$ cm^{-3}, and

$$\frac{N(\text{ortho} - H_2CO)}{\Delta v} = 10^{14}\ \text{cm}^{-2}/\text{km s}^{-1}\ ,$$

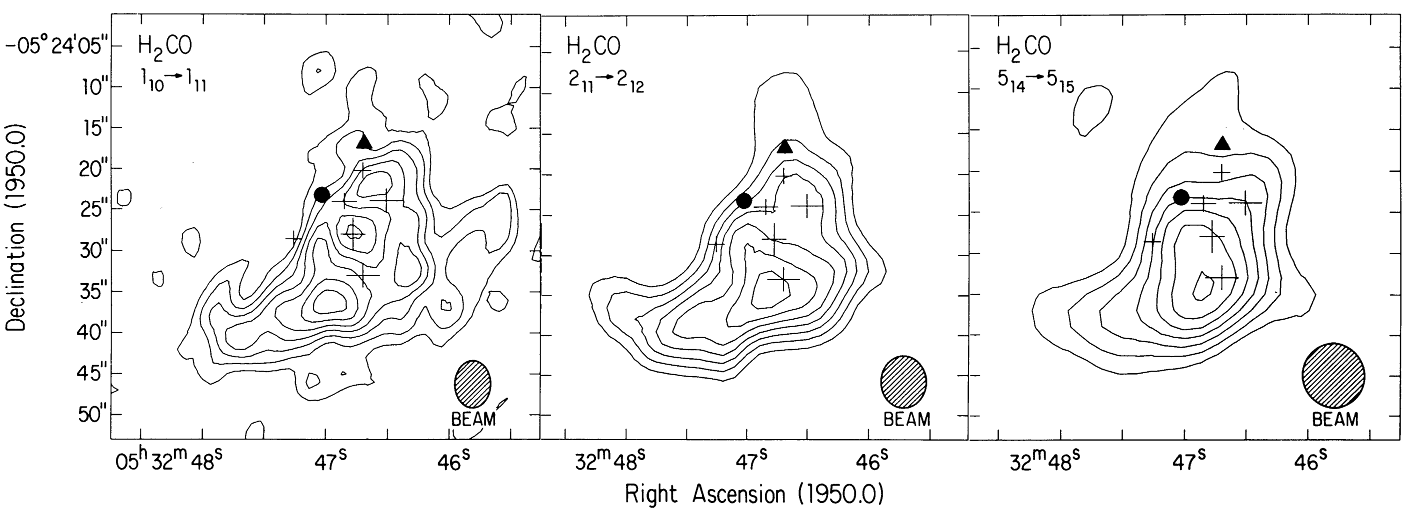

FIG. 10.—Comparison between the integrated intensities from the H_2CO $1_{10} \rightarrow 1_{11}$, $2_{11} \rightarrow 2_{12}$, and $5_{14} \rightarrow 5_{15}$ compact ridge emission distributions. The contours for all three maps are 20, 30, 40, 50, 60, 70, and 80 K km s^{-1}. The positions of the infrared sources are indicated as in Fig. 1, and the synthesized beams are shown for each transition.

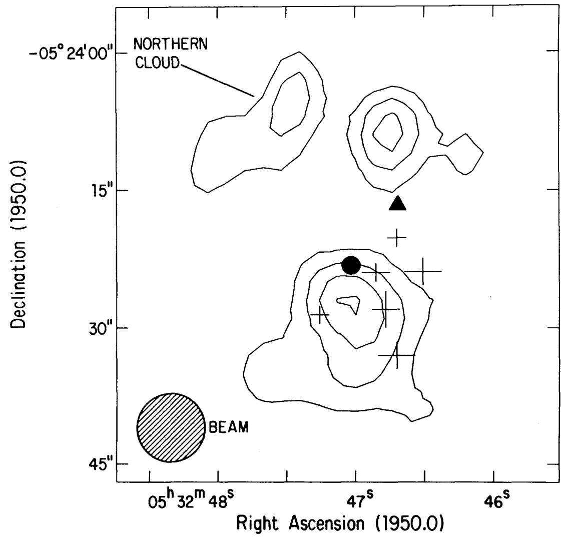

FIG. 11.—Integrated $5_{14} \rightarrow 5_{15}$ H_2CO emission from the northern cloud. The contours are 2, 3, 4, and 5 Jy beam^{-1} km s^{-1} (8, 12, 16, and 20 K km s^{-1}). The positions of the infrared sources are shown as in Fig. 1 and the synthesized beam is shown as in Fig. 6. Note that only the southwestern component of this subsource is detected.

the $J = 1$, 2, 3, and 4 K-doublets all appear in absorption at progressively weaker intensities while for $J \geq 5$ the K-doublet transitions appear in emission. Therefore, for $n(H_2) \lesssim 10^5$ cm^{-3} the $J \leq 4$ K-doublets appear in absorption while for $n(H_2) \gtrsim 10^5$ cm^{-3} all of the K-doublets which are excited appear in emission.

In addition to their selective emission properties, the K-doublets also lie at relatively low frequencies in comparison to the accompanying P-branch transitions. Therefore, the spontaneous emission rates for the K-doublets are as much as four orders-of-magnitude less than those in the P-branch transitions, which leads to much lower optical depths in the K-doublets. One can then see why the K-doublet transitions of H_2CO are such valued density probes. They are a reliable indicator of high densities, have a wide range of excitation requirements, and attain only modest optical depths even in regions with high concentrations of H_2CO.

4.2. *Modeling Procedure*

In the following, we will use the large velocity gradient (LVG) approximation to model the physical properties of the Orion-KL components. To include all transitions with significant population in the models of the warm Orion-KL components, we have used the high-temperature ortho-H_2CO excitation rates calculated by Green (1988). Due to computational limitations, these rates are calculated using He atoms as the collision partner. According to Green et al. (1978), excitation by H_2 will differ from excitation by He due to the smaller reduced mass for H_2 and differences between the interaction potentials for H_2 and He. Due to these differences, Green et al. estimate that H_2–H_2CO excitation rates should be $\sim$50% larger than those for He–H_2CO collisions. We have not applied this correction to the H_2CO excitation rates used in this analysis. In the models we include transitions up to $J = 12$, $E_u = 280$ K in the $K_{-1} = 1$ ladder and $J = 10$, $E_u = 290$ K in the $K_{-1} = 3$ ladder.

To obtain a unique solution to the spatial density, molecular column density, and kinetic temperature of a molecular cloud within the LVG model formalism, one must have measurements of at least three transitions from a molecular species. As noted in § 4.1, these transitions should be chosen to yield the highest sensitivity to the physical properties under investigation. To model the spatial density and molecular column density in the warm Orion-KL components, measurements of low optical depth transitions over a wide range of excitation are required.

Solutions produced by an LVG model can be expressed conveniently in the form of predicted radiation temperatures for the molecular transitions modeled. To minimize telescope-dependent effects (resolution, efficiency, pointing, etc.), a great deal of homogeneity within the observational data set used to constrain these models is required. This homogeneity requirement is met in the current analysis. Furthermore, to correct for the small differences in resolution (5″.9 × 4″.4 for the $1_{10} \rightarrow 1_{11}$ transition; 6″.4 × 5″.1 for the $2_{11} \rightarrow 2_{12}$ transition; 7″.9 × 7″.4 for the $5_{14} \rightarrow 5_{15}$ transition), we have convolved the $1_{10} \rightarrow 1_{11}$ and $2_{11} \rightarrow 2_{12}$ measurements to the resolution of our $5_{14} \rightarrow 5_{15}$ observations. Table 3 lists the measured radiation temperatures used in the modeling (note that T_B is free of effects due to telescope efficiency, so $T_B = T_R$).

The current analysis involves the use of three independent measurements to solve for the three variables in the models: spatial density, molecular column density, and kinetic temperature. To increase confidence in these solutions, though, it is often advantageous to have at least one degree of freedom (number of observed transitions minus the number of fit parameters). Therefore, we have simplified the models by assuming a uniform kinetic temperature within each of the individual Orion-KL components studied. We adopt the following kinetic temperatures for each component: 200 K for the hot core (Blake et al. 1987), 100 K for the compact ridge (Loren & Mundy 1984), and 50 K for the northern cloud (Plambeck & Wright 1988a).

In the following analyses, we will use two basic methods for visualizing the solutions to the spatial density and molecular column density in each Orion-KL component. The first involves a comparison of the model-predicted and observed radiation temperature as a function of H_2 density and ortho-

TABLE 3

K-DOUBLET RADIATION TEMPERATURES USED IN MODELING[a]

Component	$T_R(1_{10} \rightarrow 1_{11})$ (K)	$T_R(2_{11} \rightarrow 2_{12})$ (K)	$T_R(5_{14} \rightarrow 5_{15})$ (K)	$T_R(1_{10} \rightarrow 1_{11})/T_R(2_{11} \rightarrow 2_{12})$	$T_R(1_{10} \rightarrow 1_{11})/T_R(5_{14} \rightarrow 5_{15})$	$T_R(2_{11} \rightarrow 2_{12})/T_R(5_{14} \rightarrow 5_{15})$
Hot core	<7.2	9.6 ± 1.6	12.8 ± 4.7	<0.75	<0.56	0.75 ± 0.30
Compact ridge	38.3 ± 5.5	34.3 ± 2.8	31.6 ± 7.4	1.12 ± 0.20	1.21 ± 0.33	1.09 ± 0.27
Northern cloud	12.9 ± 4.2	15.4 ± 1.9	11.0 ± 4.2	0.84 ± 0.29	1.17 ± 0.59	0.40 ± 0.56

[a] All measurements are with respect to a 7″.9 × 7″.4 at 161°.6 beam.

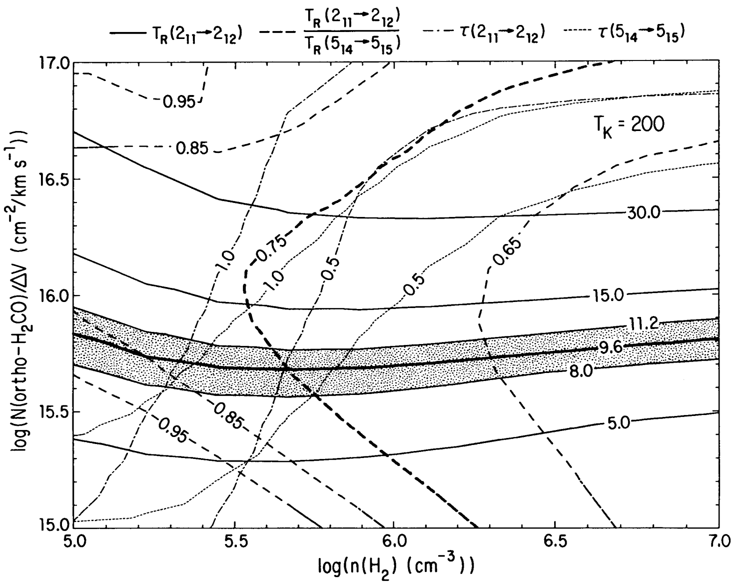

FIG. 12.—Model comparison for the H_2CO $2_{11} \to 2_{12}$ and $5_{14} \to 5_{15}$ hot core emission. Contour representations are given at the top of the diagram while the assumed model kinetic temperature is indicated in the upper right-hand corner. The stippled region represents the area in $n(H_2) - [N(\text{ortho} - H_2CO)/\Delta v]$ parameter space where solutions within $\pm 1\ \sigma$ in T_R and T_R ratio are found.

H_2CO column density per line width for each observed transition (see Fig. 12). Points of intersection between a predicted radiation temperature [like $T_R(2_{11} \to 2_{12})$] and the ratio between a pair of model-predicted radiation temperatures, like

$$\frac{T_R(2_{11} \to 2_{12})}{T_R(5_{14} \to 5_{15})},$$

define a solution to the spatial density and molecular column density in an LVG model at fixed kinetic temperature. Therefore, this kind of comparison allows us to analyze the ability of each transition to constrain the modeled molecular excitation. The second type of analysis compares all of the observed radiation temperatures with those predicted by the models to determine the region in

$$n(H_2) - \frac{N(\text{ortho} - H_2CO)}{\Delta v}$$

parameter space which contains the most probable solutions. This was done by minimizing χ^2 for each modeled component

$$\chi^2 = \sum \frac{[T_R(\text{observed}) - T_R(\text{model})]^2}{\{\sigma[T_R(\text{observed})]\}^2}.$$

The uncertainty in T_R(observed), $\sigma[T_R(\text{observed})]$ includes the rms noise in the maps and the absolute flux calibration uncertainties. When calculating $N_{TOT}(H_2CO)$ from

$$\frac{N(\text{ortho} - H_2CO)}{\Delta v}$$

one needs to multiply by the ortho:para ratio (assumed 3:1) and the line width. Since the uncertainties in $N_{TOT}(H_2CO)$ are dominated by other factors in the analysis, we have not included errors in line width determination in the quoted uncertainties. Excitation curves (cf. Fig. 13) and χ^2 diagrams (cf. Fig. 16) form the visualization of this second type of analysis.

There is one additional observational constraint which can be applied to the model. Based on a lower limit to the dust continuum flux (Mundy et al. 1986) and upper limits to the distance (Genzel et al. 1981) and source size, we estimate an absolute lower limit to the spatial density of 10^5 cm^{-3} in each of the Orion-KL components. Therefore, in modeling each component we consider only densities above this limit.

4.2.1. *Hot Core*

In Figures 12 and 13 we show the results from our LVG model fits to the Orion-KL hot core. Because we have only an upper limit to the peak radiation temperature of the $1_{10} \to 1_{11}$ transition from this component, only the $2_{11} \to 2_{12}$ and

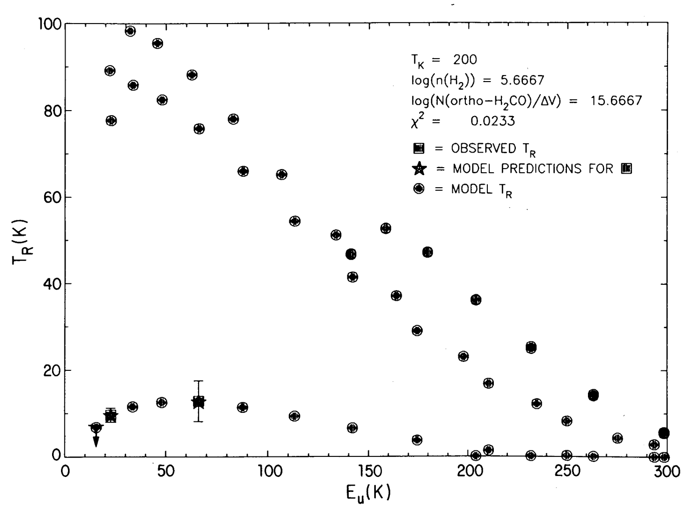

FIG. 13.—Hot core H_2CO excitation curve. Predicted radiation temperatures for all transitions included in the best-fit model are plotted as a function of the energy of the upper state for each transition. The best-fit H_2 density, ortho-H_2CO column density per line width, and the χ^2 of the fit are indicated in the upper right. The observed peak *K*-doublet radiation temperatures are also indicated.

$5_{14} \rightarrow 5_{15}$ transitions have been used to constrain the model solutions. As Figures 12 and 13 show, the best-fit model for

$$T_R(2_{11} \rightarrow 2_{12}) = 9.6 \text{ K} ,$$

$$\frac{T_R(2_{11} \rightarrow 2_{12})}{T_R(5_{14} \rightarrow 5_{15})} = 0.75 ,$$

and $T_K = 200$ K implies

$$n(H_2) = 10^{5.7} \text{ cm}^{-3} ,$$

$$\frac{N(\text{ortho} - H_2CO)}{\Delta v} = 10^{15.7} \text{ cm}^{-2}/\text{km s}^{-1} ,$$

and

$$\tau(2_{11} \rightarrow 2_{12}) \simeq \tau(5_{14} \rightarrow 5_{15}) \simeq 0.5 .$$

Unfortunately, the models are not well constrained by these two transitions and, within $\pm 1\ \sigma$ in $T_R(2_{11} \rightarrow 2_{12})$ and

$$\frac{T_R(2_{11} \rightarrow 2_{12})}{T_R(5_{14} \rightarrow 5_{15})} ,$$

acceptable solutions exist for $n(H_2) \gtrsim 10^5$ cm^{-3} and

$$\frac{N(\text{ortho} - H_2CO)}{\Delta v} = 10^{15.7^{+0.2}_{-0.1}} \text{ cm}^{-2}/\text{km s}^{-1} .$$

The fact that the K-doublet optical depths are small in these models indicates that they are good spatial density probes. But, because of its high density and temperature, measurements of higher-excitation K-doublets are required to accurately model the Orion-KL hot core. This is apparent in Figure 13, where the model radiation temperatures only begin to drop near the $J = 7$ level in the K-doublet transitions.

4.2.2. *Compact Ridge*

The LVG model fits to the observed peak K-doublet radiation temperatures toward the compact ridge are shown in Figures 14 and 15. There are several points worth noting about these comparisons:

1. $\tau(1_{10} \rightarrow 1_{11}) < \tau(2_{11} \rightarrow 2_{12}) < \tau(5_{14} \rightarrow 15_{15}) \lesssim 3$ for the best-fit solutions to $n(H_2)$ and

$$\frac{N(\text{ortho} - H_2CO)}{\Delta v}$$

in these diagrams. This increase in τ through the K-doublets is due primarily to the increase in the spontaneous emission coefficient for the higher frequency transitions. One would think that since all three transitions are reaching moderate ($\sim$1–3) optical depths in these solutions, they must have lost some sensitivity to spatial density. The fact that all three best-fit solutions are the same, though, indicates that these transitions do retain much of their spatial density sensitivity in the compact ridge.

2. At values of the brightness temperature ratios one standard deviation above the nominal values, the solution to $n(H_2)$ are below our absolute lower limit of 10^5 cm^{-3} (see § 4.2). For these solutions, $\tau \gg 1$ and all three K-doublet transitions lose sensitivity to spatial density.

3. The best-fit spatial density and ortho-H_2CO column density per line width are approximately the same in all three comparisons: $n(H_2) \simeq 10^{5.4}$ cm^{-3} and

$$\frac{N(\text{ortho} - H_2CO)}{\Delta v} \simeq 10^{16.4} \text{ cm}^{-2}/\text{km s}^{-1} .$$

Using the χ^2 analysis described above, $n(H_2) = 10^{5.5^{+0.8}_{-0.5}}$ cm^{-3} and

$$\frac{N(\text{ortho} - H_2CO)}{\Delta v} = 10^{16.4^{+0.4}_{-0.2}} \text{ cm}^{-2}/\text{km s}^{-1}$$

within a 98% (3 σ) confidence limit (Fig. 16).

4. The model excitation curve representing the lowest value of χ^2 is shown in Figure 17. Since the observed K-doublet transitions sample only the low-excitation portion of this distribution, the LVG models describe only the lower densities in the compact ridge.

By forming ratios of the radiation temperature maps at $V_{LSR} = 8$ km s^{-1} between each of the K-doublet transitions we

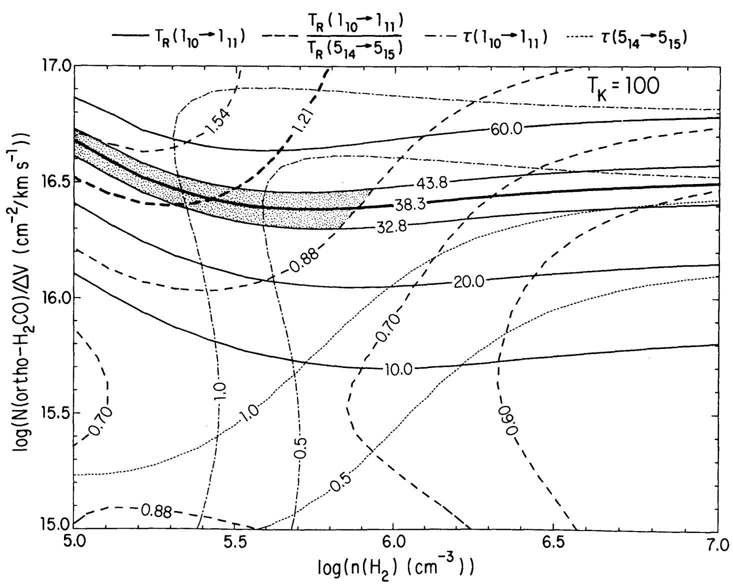

FIG. 14.—Model comparison for the H_2CO $1_{10} \rightarrow 1_{11}$ and $5_{14} \rightarrow 5_{15}$ compact ridge emission. The annotation is the same as that in Fig. 12

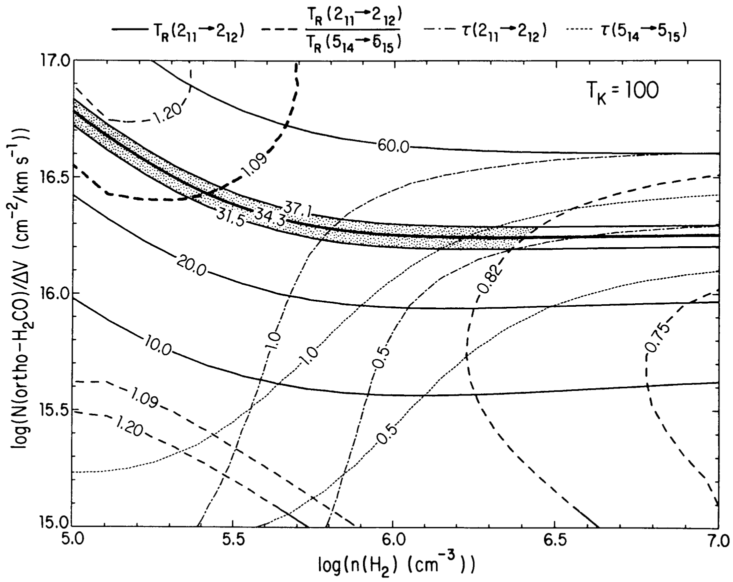

FIG. 15.—Model comparison for the H_2CO $2_{11} \rightarrow 2_{12}$ and $5_{14} \rightarrow 5_{15}$ compact ridge emission. The annotation is the same as that in Fig. 12

have also investigated the density structure in the compact ridge. Over regions in which the brightness temperatures in all three of the K-doublet transitions are greater than twice the rms noise in the maps, with few exceptions the radiation temperature ratios vary between 0.75 and 1.25. In the few places where the radiation temperature ratio is measured to be out of this range, it is always greater than 1.25. Since the measured T_R in these regions is correspondingly low, the LVG models would predict a very low density and a very high column density per line width. But, because a change in density can be compensated for by a change in kinetic temperature, which has been fixed in these models, factor of 2 changes in T_K can also produce the observed variations. Therefore, we can only conclude that the uniformity in the radiation temperature ratios suggests a uniform spatial density over the compact ridge and that isolated regions where this uniformity is interrupted could be caused by small changes in either density or temperature.

Comparing our high-resolution H_2CO LVG model of the compact ridge to the model of Mangum et al. (1990), we find good agreement. Using observations of many of the $K_{-1} =$ 1 and 3 transitions of H_2CO, $H_2^{13}CO$, and $H_2C^{18}O$ between 211 and 352 GHz at 1′ resolution, Mangum et al. derived $n(H_2) = 10^{6.8^{+0.2}_{-0.1}}$ cm^{-3} and

$$\frac{N(\text{ortho} - H_2CO)}{\Delta v} = 10^{14.7^{+0.2}_{-0.1}}\ \text{cm}^{-2}/\text{km s}^{-1}\ .$$

After scaling the Mangum et al.–derived

$$\frac{N(\text{ortho} - H_2CO)}{\Delta v}$$

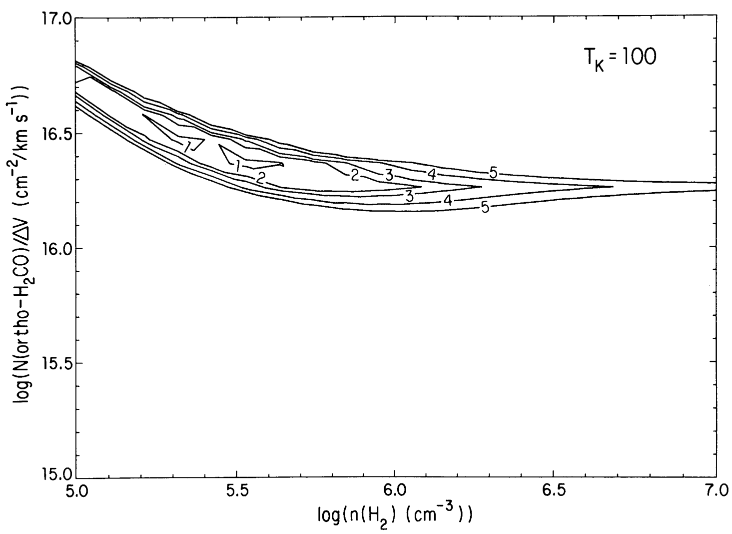

FIG. 16.—Model χ^2 distribution for the compact ridge. Contours are given in units of the standard deviation (σ) while the assumed model kinetic temperature is indicated in the upper right-hand corner.

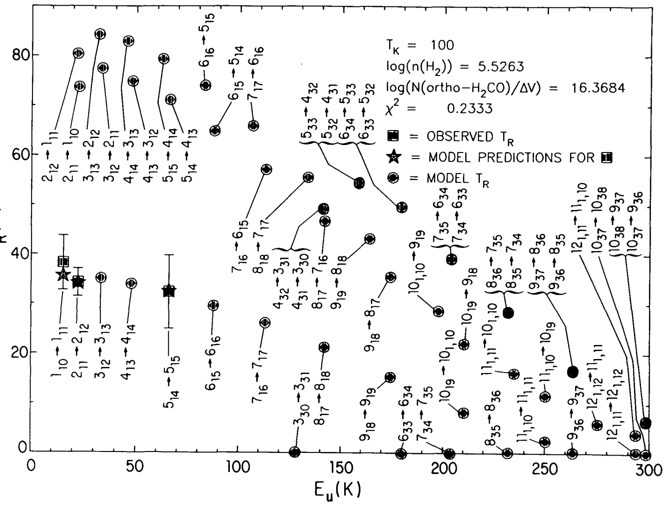

FIG. 17.—Compact ridge H_2CO excitation curve. The annotation is the same as that in Fig. 13 except that the modeled transitions are explicitly indicated.

by the ratio of the single antenna source size and interferometric beam area, we find excellent agreement between the single antenna and interferometer results. We should point out, though, that the H_2CO transition optical depths estimated by Mangum et al. are 2–20 times lower than those derived in the present analysis. This underestimate was likely due to uncertainties in the corrections for beam dilution and source coupling efficiency used by Mangum et al. Note that the spatial density estimated by Mangum et al. is unaffected by this underestimate of the transition optical depths. The LVG solution presented in that analysis was partially constrained by measurements of less-opaque transitions from $H_2^{13}CO$ and $H_2C^{18}O$, making it less dependent upon uncertainties in the H_2CO transition optical depths.

The spatial density derived by Mangum et al. is approximately an order-of-magnitude larger than the value we have derived in our K-doublet models. This difference is due to the fact that Mangum et al. used transitions ranging in excitation from $E_u = 21.0$ to 14.1 K, while the K-doublet models presented here were constrained by transitions in a somewhat lower ($E_u = 15.8$ to 65.9 K) range of excitation. The Mangum et al. models also included some optically thick P-branch transitions. As noted by Mangum et al., below $n(H_2) \sim 10^6$ cm^{-3} the $K_{-1} = 3$ transitions in their models become quite weak, while at $n(H_2) \sim 5 \times 10^7$ cm^{-3} the $K_{-1} = 3$ transitions rapidly approach the intensity of the $K_{-1} = 1$ transitions. Therefore, the higher excitation, lower optical depth $K_{-1} = 3$ transitions pushed the Mangum et al. models to higher densities. To show that the low-resolution and high-resolution models are at least consistent, we present in Figure 18 LVG model fits to $T_R(2_{11} \rightarrow 2_{12})$ and

$$\frac{T_R(2_{11} \rightarrow 2_{12})}{T_{R}(5_{14} \rightarrow 5_{15})}$$

using both the high-resolution radiation temperatures and these radiation temperatures convolved to a resolution of 1′. The convolved radiation temperatures are best fit by a spatial density of $10^{5.9}$ cm^{-3}, consistent with the interferometer model fits above.

4.2.3. *Northern Cloud*

In Figures 19 and 20 we display the LVG model fits to the peak K-doublet radiation temperatures observed toward the Orion-KL northern cloud. The best-fit spatial density and ortho-H_2CO column density per line width in each comparison ranges from $10^{5.6}$ cm^{-3} and $10^{15.6}$ cm^{-2}/km s^{-1} to $10^{6.2}$ cm^{-3} and $10^{15.7}$ cm^{-2}/km s^{-1}. Unfortunately, the K-doublet H_2CO emission from this component is less than half as strong as it is in the compact ridge, which causes our spatial density measurement uncertainties to be rather large. Within our 98% (3 σ) confidence limits in χ^2 (Fig. 21), $n(H_2)$ is not well determined [$n(H_2) \gtrsim 10^5$ cm^{-3}]; only for confidence limits $\lesssim$80%

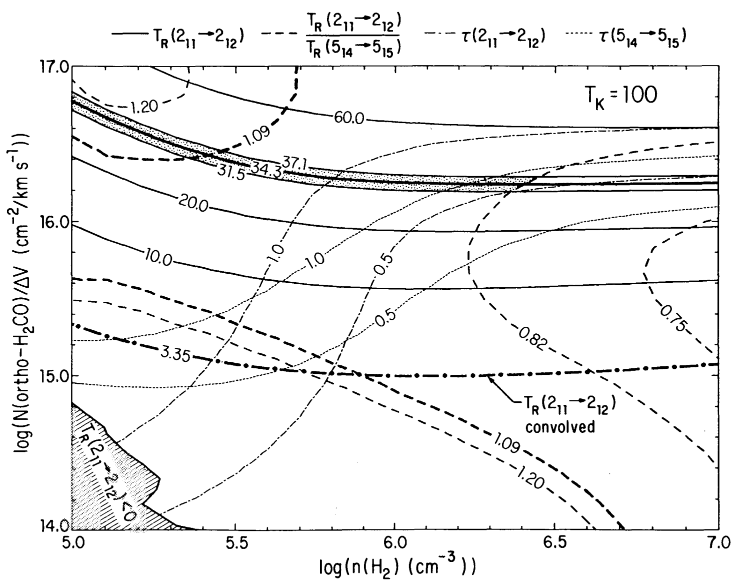

FIG. 18.—Model comparison for the H_2CO $2_{11} \rightarrow 2_{12}$ and $5_{14} \rightarrow 5_{15}$ compact ridge emission. This diagram differs from Fig. 15 in that solutions over a larger range in column density are shown. The convolved H_2CO $2_{11} \rightarrow 2_{12}$ radiation temperature is shown, and otherwise the annotation is the same as that in Fig. 15.

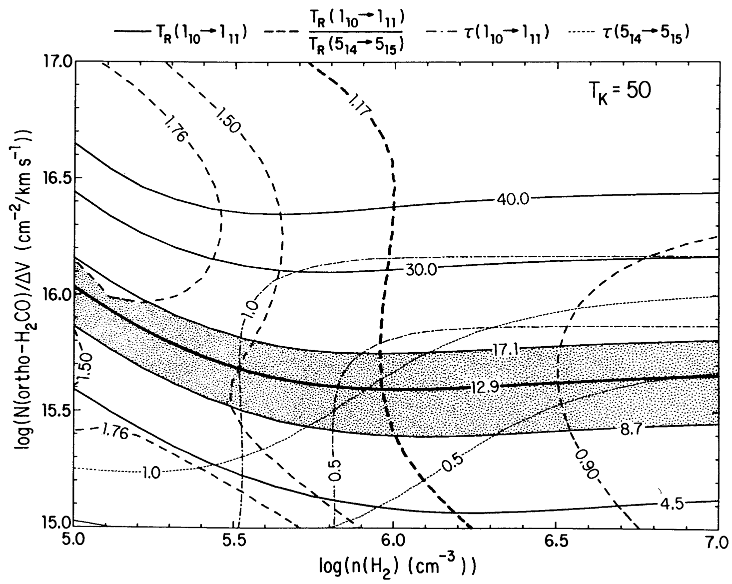

FIG. 19.—Model comparison for the H_2CO $1_{10} \rightarrow 1_{11}$ and $5_{14} \rightarrow 15_{15}$ northern cloud emission. The annotation is the same as that in Fig. 12

do the models constrain $n(H_2)$. Within a 68% (1 σ) confidence limit, $n(H_2) = 10^{5.9^{+0.7}_{-0.5}}$ cm^{-3} and

$$\frac{N(\text{ortho}-H_2CO)}{\Delta v} = 10^{15.6^{+0.3}_{-0.1}} \text{ cm}^{-2}/\text{km s}^{-1} .$$

Clearly, the spatial density in the northern cloud is similar to that measured in the compact ridge but the ortho-H_2CO molecular column density per line width is ~5 times lower than that measured in the compact ridge.

Even though the northern cloud is a relatively quiescent (in comparison to the hot core and compact ridge) condensation in the northern portion of the Orion molecular ridge, as noted in § 3.2.3, $5_{14} \rightarrow 5_{15}$ H_2CO emission is detected only in the southwestern, dynamically interactive component of what appears to be a two-component structure in the $1_{10} \rightarrow 1_{11}$ and $2_{11} \rightarrow 2_{12}$ H_2CO emission. Therefore, the model presented above defines only the southwestern portion of this source.

As is apparent from the LVG model spectrum for this component (Fig. 22), the three K-doublet transitions used to constrain the models do an excellent job of sampling the excitation of H_2CO in this source. Since the $5_{14} \rightarrow 5_{15}$ transition lies approximately $\frac{1}{3}$ of the way down the tail of the excitation distribution, one might expect the strength of this transition to show some sensitivity to the kinetic temperature in the northern cloud. To test this supposition, we have constructed LVG models over $n(H_2) = 10^5$–10^7 cm^{-3},

$$\frac{N(\text{ortho}-H_2CO)}{\Delta v} = 10^{15}\text{–}10^{17} \text{ cm}^{-2}/\text{km s}^{-1} ,$$

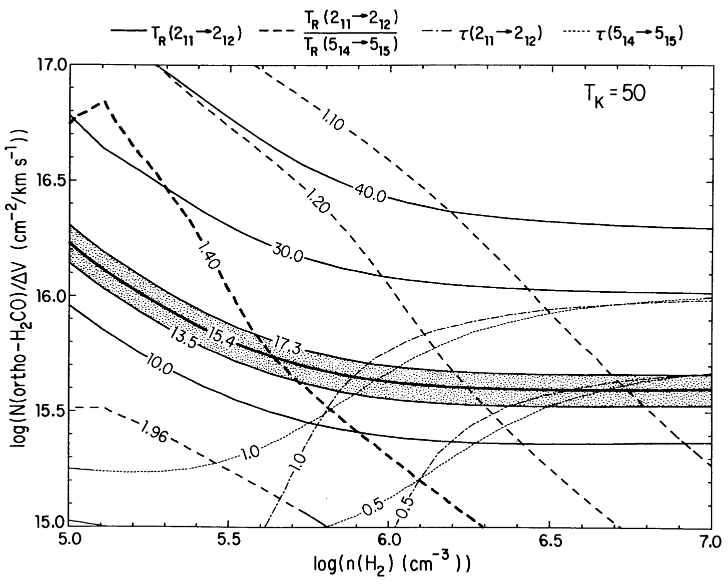

FIG. 20.—Model comparison for the H_2CO $2_{11} \rightarrow 2_{12}$ and $5_{14} \rightarrow 5_{15}$ northern cloud emission. The annotation is the same as that in Fig. 12

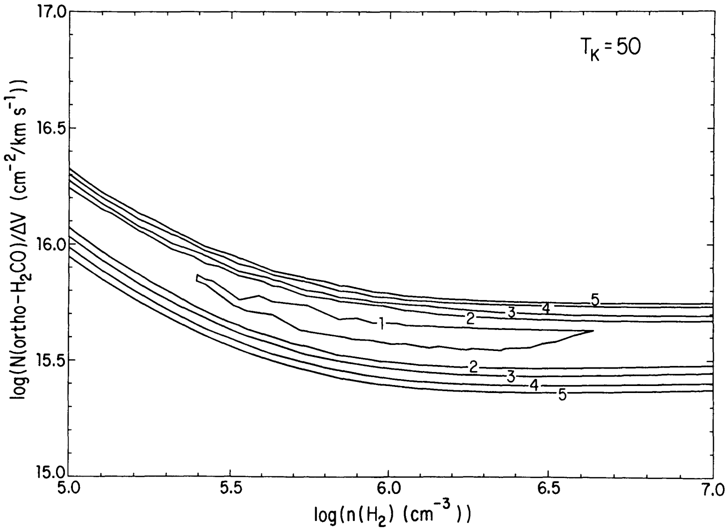

FIG. 21.—Model χ^2 distribution for the northern cloud. The annotation is the same as that in Fig. 16

and $T_K = 20$–150 K. As expected, models at $T_K \gtrsim 60$ K overpredict $T_R(5_{14} \rightarrow 5_{15})$ while models at $T_K \lesssim 40$ K underpredict $T_R(5_{14} \rightarrow 5_{15})$. Therefore, the transitions used in this analysis do an excellent job of constraining the LVG models of the warm gas in the northern cloud.

4.3. *Model Synopsis*

Table 4 is a summary of our LVG model results for the Orion-KL hot core, compact ridge, and northern cloud. As the model excitation curves indicate (Figs. 13, 17, and 22), the three *K*-doublet transitions used in this analysis are sensitive only to the lower excitation ($T_K \lesssim 100$ K) regions in these subsources. Therefore, our models are good representations of the moderate [$10^5 \lesssim n(H_2) \lesssim 10^6$ cm^{-3}] spatial densities in the hot core and compact ridge. For the coolest of the Orion-KL subsources, the northern cloud, the three *K*-doublet transitions do a good job of sampling all of the H_2CO excitation (see Fig. 22). Our LVG model fit to these observations is therefore a good representation of the average spatial density and H_2CO column density in the northern cloud.

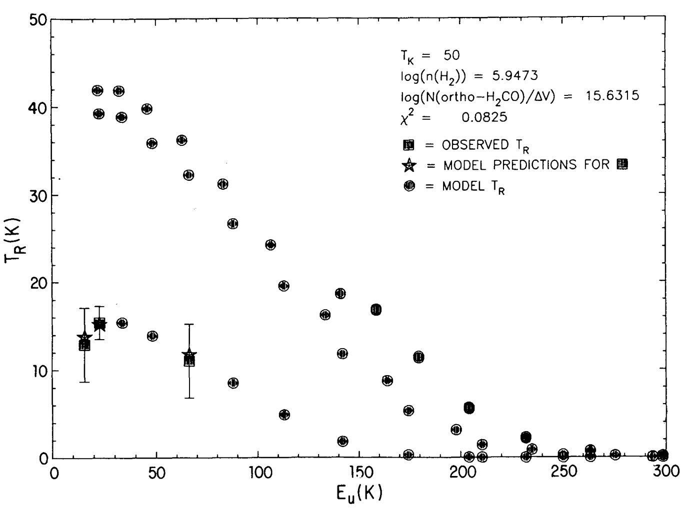

FIG. 22.—Northern cloud H_2CO excitation curve. The annotation is the same as that in Fig. 13.

In the compact ridge, it appears that the H_2CO abundance is large enough to bring about moderate optical depths in these transitions. We are still able to obtain an estimate of the spatial density in this region, but a significant contribution to the uncertainty in this estimate is due to the increased optical depth in these transitions.

We have also calculated the H_2CO abundances, X(H_2CO), for each of the Orion-KL subsources (Table 4). As noted by Mangum et al. (1990), molecular species which are thought to be primary constituents of icy grain mantles (NH_3, CH_3OH, H_2CO, etc.; see Tielens & Allamandola 1987a, b; Charnley, Tielens, & Miller 1992) are at least 10 times more abundant than CS and HC_3N, which are not suspected to be easily liberated from grains. The case for the involvement, both passively and actively, of grains in H_2CO chemistry has recently become stronger with the detection of D_2CO in the compact ridge (Turner 1990). Therefore, an attractive scenario which explains the large H_2CO abundances is one in which the high rate of massive star formation in the Orion-KL region has led to the release of H_2CO from the surfaces of icy grain mantles.

5. CONCLUSIONS

High-resolution ($\theta_B \simeq 5''$–$8''$, or 2500–4000 AU) observations of the $1_{10} \rightarrow 1_{11}$ and $5_{14} \rightarrow 5_{15}$ transitions of H_2CO have been made of the Orion-KL star-forming region. By combining these observations with 6″ resolution measurements of the $2_{11} \rightarrow 2_{12}$ transition (Mangum et al. 1990), we have applied a spherical LVG model of the H_2CO excitation to derive the H_2 density and H_2CO column density in the Orion-KL hot core, compact ridge, and northern cloud.

1. The Orion-KL hot core is a strong emitter in the H_2CO $5_{14} \rightarrow 5_{15}$ transition, but is comparatively weak in the $1_{10} \rightarrow 1_{11}$ transition. This is a consequence of the high kinetic temperature in this component. The best-fit H_2 density and H_2CO column density from our LVG models of this source are $10^{5.7}$ cm^{-3} and $10^{16.9}$ cm^{-2}, respectively. Unfortunately, this best-fit spatial density is unconstrained toward higher spatial densities. Because the measured transitions used to constrain the LVG models have low excitation requirements, we have

TABLE 4

LARGE VELOCITY GRADIENT MODEL RESULTS

		log $[n(H_2)]$[a]			log $[N(H_2CO)]$[a,b]			
COMPONENT	ASSUMED T_K (K)	Best-fit (cm^{-3})	1 σ (cm^{-3})	3 σ (cm^{-3})	Best-fit (cm^{-3})	1 σ (cm^{-3})	3 σ (cm^{-3})	$X(H_2CO)$[c]
Hot core	200	5.7	...	...	16.9	...	...	−7.4
Compact ridge	100	5.5	$5.5^{+0.2}_{-0.3}$	$5.5^{+0.8}_{-0.5}$	17.2	$17.2^{+0.2}_{-0.1}$	$17.2^{+0.4}_{-0.2}$	−6.8
Northern cloud	50	5.9	$5.9^{+0.7}_{-0.5}$	>5	16.0	$16.0^{+0.3}_{-0.1}$	$16.0^{+0.7}_{-0.3}$	−8.0

[a] Values given are for the best-fit solution and the solutions within 1 σ and 3 σ as determined from a χ^2 analysis (see § 4.3).

[b] Model $N(\text{ortho} - H_2CO)/\Delta v$ have been multiplied by 4/3 to correct for ortho-para splitting and by $\Delta v = 10.9$, 4.4, and 1.9 km s^{-1} (the average line width from our three K-doublet measurements) for each component to get $N(H_2CO)$.

[c] Calculated using best fit $N(H_2CO)$ and $N(H_2) = 2 \times 10^{24}$ cm^{-2} for the hot core and 1×10^{24} cm^{-2} for the compact ridge and northern cloud (derived from data in Mundy et al. 1986).

not adequately sampled the majority of the hot core molecular material. Therefore, our derived H_2 density is *not* the peak density in the hot core.

2. The compact ridge component in Orion-KL is the dominant H_2CO emission feature in all three *K*-doublet transitions. As was the case in our LVG models of the hot core, the measured *K*-doublet transitions sample only the lower excitation, lower density gas in this warm region. We also find that the large H_2CO abundance in the compact ridge has caused the optical depth in the measured *K*-doublet transitions to reach moderate values. The best-fit H_2 density and H_2CO column density are $10^{5.5}$ cm^{-3} and $10^{17.2}$ cm^{-2}, respectively. A comparison of the spatial distribution of the *K*-doublet emission regions indicates that the compact ridge has a uniform spatial density over most of its area. Comparison with the lower resolution, higher excitation H_2CO models of Mangum et al. (1990) has shown that a dependence on low-excitation molecular transitions to model the physical conditions in warm molecular clouds will bias derived densities toward lower values.

3. The best-fit H_2 density and H_2CO column density for the northern cloud are $10^{5.9}$ cm^{-3} and 10^{16} cm^{-2}, respectively. The *K*-doublet measurements toward this component do an excellent job of sampling the H_2CO excitation, but because the emission is relatively weak, measurement uncertainties make it difficult to constrain the modeled H_2 density and H_2CO column density.

4. The large abundances of H_2CO measured in the hot core and compact ridge, coupled with the high level of deuterium fractionation in these sources, implies that grain mantle sublimitation is a significant contributor to the H_2CO abundance.

5. For the astrophysicist who wants to accurately measure the spatial density and H_2CO column density in dense star-forming regions, the *K*-doublet transitions of H_2CO present the perfect tool. Accessibility over a wide range in excitation, low optical depth even in the H_2CO-rich Orion-KL region, and the fact that the existence of *K*-doublet emission implies $n(H_2) \gtrsim 10^5$ cm^{-3} leads to the ultimate utility of these transitions for deriving the physical conditions in molecular clouds. Even though these transitions are often too weak to be measureable, the next generation of radio telescopes operating at centimeter and millimeter wavelengths should make the *K*-doublet transitions of H_2CO readily detectable in many star-forming regions.

We thank the referee, Lee Mundy, for useful comments and suggestions which significantly improved this paper. J. G. M. would like to thank the National Radio Astronomy Observatory for support through a Junior Research Associateship. This work was supported in part by Texas Advanced Research Program grant 003658-285 and National Science Foundation grant AST 90-17710 to the University of Texas. The BIMA observations were supported in part by NSF grant AST 87-14721.

REFERENCES

Bastien, P., Batrla, W., Henkel, C., Pauls, T., Walmsley, C. M., & Wilson, T. L. 1985, A&A, 146, 86
Batrla, W., Wilson, T. L., Bastien, P., & Ruf, K. 1983, A&A, 128, 279
Blake, G. A., Sutton, E. C., Masson, C. R., & Phillips, T. G. 1986, ApJS, 60, 357
———. 1987, ApJ, 315, 621
Charnley, S. B., Tielens, A. G. G. M., & Millar, T. J. 1992, preprint
Churchwell, E., Felli, M., Wood, D. O. S., & Massi, M. 1987, ApJ, 321, 516
Downes, D., Genzel, R., Becklin, E. E., & Wynn-Williams, C. G. 1981, ApJ, 244, 869
Downes, D., Wilson, T. L., Bieging, J., & Wink, J. 1980, A&AS, 40, 379
Evans, N. J., II, Zuckerman, B., Morris, G., & Sato, T. 1975, ApJ, 196, 433
Garrison, B. J., Lester, W. A., Miller, W. H., & Green, S. 1975, ApJ, 200, L175
Genzel, R., Reid, M. J., Moran, J. M., & Downes, D. 1981, ApJ, 244, 884
Greason, M. R. 1986, thesis, Univ. Virginia
Green, S. 1988, private communication
Green, S., Garrison, B. J., Lester, W. A., Jr., & Miller, W. H. 1978, ApJS, 37, 321
Jewell, P. R., Hollis, J. M., Lovas, F. J., & Snyder, L. E. 1989, ApJS, 70, 833
Johansson, L. E. B., et al. 1984, A&A, 130, 227
Johnston, K. J., Palmer, P., Wilson, T. L., & Bieging, J. H. 1983, ApJ, 271, L89
Keene, J., Hildebrand, R. H., & Whitcomb, S. E. 1982, ApJ, 252, L11
Kleinmann, D. E., & Low, F. J. 1967, ApJ, 149, L1
Loren, R. B., & Mundy, L. G. 1984, ApJ, 286, 232
Mangum, J. G., Plambeck, R. L., & Wootten, A. 1991, ApJ, 369, 169
Mangum, J. G., Wootten, A., Loren, R. B., & Wadiak, E. J. 1990, ApJ, 348, 542
Masson, C. R., Lo, K. Y., Phillips, T. G., Sargent, A. I., Scoville, N. Z., & Woody, D. P. 1987, ApJ, 319, 446
Mundy, L. G., Cornwell, T. J., Masson, C. R., Scoville, N. Z., Bååth, L. B., & Johansson, L. E. B. 1988, ApJ, 325, 382
Mundy, L. G., Scoville, N. Z., Bååth, L. B., Masson, C. R., & Woody, D. P. 1986, ApJ, 304, L51
Plambeck, R. L., & Wright, M. C. H. 1988a, in Molecular Clouds in the Milky Way and External Galaxies, ed. R. L. Dickman, R. L. Snell, & J. S. Young (Heidelberg: Springer), 182
———. 1988b, ApJ, 330, L61
Plambeck, R. L., Wright, M. C. H., Welch, W. J., Bieging, J. H., Baud, B., Ho, P. T. P., & Vogel, S. N. 1982, ApJ, 259, 617
Sutton, E. C., Blake, G. A., Masson, C. R., & Phillips, T. G. 1985, ApJS, 58, 341
Thaddeus, P., Kutner, M. L., Penzias, A. A., Wilson, R. W., & Jefferts, K. B. 1972, ApJ, 176, L73
Tielens, A. G. G. M., & Allamandola, L. J. 1987a, in Physical Processes in Interstellar Clouds, ed. G. E. Morfill & M. Scholer (Dordrecht: Reidel), 333
———. 1987b, in Interstellar Processes, ed. D. J. Hollenbach & H. QA. Thronson, Jr. (Dordrecht: Reidel), 397
Turner, B. E. 1989, ApJS, 70, 539

Turner, B. E. 1990, ApJ, 362, L29
Vogel, S. N., Bieging, J. H., Plambeck, R. L., Welch, W. J., & Wright, M. C. H. 1985, ApJ, 296, 600
Werner, M. W., Gatley, I., Harper, D. A., Becklin, E. E., Loewenstein, R. F., Telesco, C. M., & Thronson, H. A. 1976, ApJ, 204, 420
Wilson, R. W., Jefferts, K. B., & Penzias, A. A. 1970, ApJ, 161, L43
Wilson, T. L., & Pauls, T. A. 1984, A&A, 138, 225
Wilson, T. L, Serabyn, E., Henkel, C., & Walmsley, C. M. 1986, A&A, 158, L1
Wootten, A., & Loren, R. B. 1984, ApJ, 277, 189
Wright, M. C. H., Plambeck, R. L., Vogel, S. N., Ho, P. T. P., & Welch, W. J. 1983, ApJ, 267, L41
Wynn-Williams, C. G., Genzel, R., Becklin, E. E., & Downes, D. 1984, ApJ, 281, 172
Ziurys, L. M., Wilson, T. L., & Mauersberger, R. 1990, ApJ, 356, L25
Zuckerman, B., Kuiper, T. B. H., & Rodriguez–Kuiper, E. N. 1976, ApJ, 209, L137
Zuckerman, B., Palmer, P., & Rickard, L. J. 1975, ApJ, 197, 571